PLEASE: an Open-Source Emulation Platform for Development of Sustainable and Battery-Less Sensor Systems

Jelle Jocqué, Michiel Matthijs, Dries Van Leemput, Eli De Poorter, Jo Verhaevert, *Member, IEEE*, Patrick Van Torre, *Member, IEEE*, Hendrik Rogier, *Senior Member, IEEE*

***Abstract*—Driven by the increasing demand for data, connectivity and automation, the amount of Internet of Things (IoT) devices continues to expand across consumer electronics and industrial applications. Integrating energy harvesting (EH) technologies as a battery-free alternative requires a controlled setting to emulate realistic energy harvesting systems. Yet, current tools are often not sufficiently accurate to model all hardware and software components of an EH system. Moreover, it is hard to mimic realistic energy availability scenarios, which are crucial for the design and optimization of EH systems. Therefore, a novel emulation platform is introduced that facilitates the development, testing, and optimization of complete and realistic EH systems. This emulator device replicates the behavior of the entire EH system. It consists of a Raspberry Pi 5 with a custom developed add-on hardware hat and dedicated software. This add-on hardware hat provides a stable output voltage between 1.2 V and 3.6 V to the IoT device under test and contains a current measurement circuit with an accuracy of 0.6 µA. The software includes novel and accurate digital-twin models of the energy harvester, the storage element, and the power management unit, enabling the emulation of various EH scenarios. Two application scenarios are demonstrated, a wireless Bluetooth Low Energy (BLE) heart rate sensor optimized for ambient light EH and a compact wireless BLE temperature sensor optimized for radio-frequency EH. The proposed emulation platform enables rapid EH design evaluation under varying energy conditions, streamlining development and validating system reliability. This could be an important step toward establishing EH as a sustainable and widely adopted alternative to conventional battery-powered systems.**

***Index Terms*—Energy Harvesting, IoT, Emulation Platform, Solar Cell, Power Management Unit, Supercapacitor**

I. Introduction

EVERY day, electronic devices become smarter and more interconnected, altering the way we interact with them. These devices are part of the broader ecosystem known as the Internet of Everything (IoE), which extends beyond the traditional Internet of Things (IoT) by integrating not only physical objects and sensors but also people, processes, and data into a unified network. This network covers everything from smart home appliances and energy-efficient systems to tracking wildlife and even locating misplaced items. However, most IoT devices today still rely on wired connections or batteries. In response to sustainability concerns, energy harvesting (EH) technologies are gaining more attention as an alternative power source for these devices. EH captures ambient energy for storage in small batteries or supercapacitors, offering an eco-friendlier alternative to the extraction of lithium and rare-earth materials.

Despite its potential, the market for EH remains a limited fraction of the overall IoT market. Sectors such as "Building and home automation" and "Consumer electronics" show the greatest growth potential for EH technology [1]. However, challenges such as fluctuations in energy availability have led to perceptions of unreliability, preventing the broader adoption of EH technology. This is reflected in the slower growth rate of EH systems within the IoT market, being a Compound Annual Growth Rate (CAGR) of only 8%, compared to the overall IoT market's CAGR of 20% [1], [2].

Making EH a viable alternative in different environments requires a controlled setup to emulate realistic system behavior. Such an emulation platform should integrate diverse energy sources, energy conversion processes and storage elements. Thereby, it will enable companies to adopt EH technologies without spending large amounts of resources. Existing tools often fail to accurately model all components of a complete EH system. Moreover, they cannot fully mimic realistic energy availability scenarios, which is crucial for the design and optimization of EH systems. A fast and accurate emulation platform would enable designers to optimize hardware and software early in the design cycle, significantly accelerating the time to market. For example, for battery replacement, a designer might initially size the supercapacitor and energy harvester based on worst-case scenarios [3]. By exploiting the emulation platform, the designer has access to a controlled, experiment-driven environment with the capability to produce repeatable data. In turn, this facilitates hardware and software optimization to better cope with the limited power availability. This approach enables rapid evaluation of the viability of a product, ensuring that choices are well-informed and efficient.

Therefore, this paper describes and validates a novel open-source emulation platform, called PLEASE: Portable Laboratory for Energy Acquisition and Storage Emulation. This emulation platform is designed to deliver fast and accurate results without requiring specific EH hardware or pre-captured

Manuscript received April 13, 2025; revised June 26, 2025; accepted July 31, 2025; date of current version July 31, 2025. *(Corresponding author: Jelle Jocqué.)*

Jelle Jocqué, Michiel Matthijs, Dries Van Leemput, Eli De Poorter, Jo Verhaevert, Patrick Van Torre and Hendrik Rogier are with the Department of Information Technology, Ghent University/imec, 9052 Ghent, Belgium (e-mail: jelle.jocque@ugent.be).

data. It employs a digital-twin model of the harvester, the storage element and the power management unit (PMU), requiring only the device under test (DUT) and a Raspberry Pi (RPI) single-board computer with a custom add-on hardware hat. This add-on hardware hat provides a programmable and stable output voltage between 1.2 V and 3.6 V, making it suitable for powering a wide range of wireless sensor network (WSN) applications. Additionally, it includes a current measurement circuit capable of handling currents from 1 µA to 0.6 A, corresponding to the current requirements of WSN applications, transitioning from deep-sleep mode to active data transmission. The entire system is integrated with an RPI 5 with 8 GB RAM, providing also the graphical user interface (GUI).

Specifically, the key contributions of this paper are the following:

1) **Digital-Twin Integration**: An accurate and realistic digital-twin model of each part of a typical EH system.
   - Convenient emulations models for indoor and outdoor photovoltaic (PV) cells based on basic properties.
   - Possibility to emulate rectifiers and rectenna systems based on measured or simulated current-voltage (I-V) curves.
   - Complete and realistic model of the PMU with integrated buck-boost converter and low-dropout regulator (LDO) converter, and maximum power point (MPP) functionality.
   - Novel and advanced supercapacitor model integrating the Law of Coulomb, leakage current and diffusion current characteristics.
2) **Add-on Hardware Hat**: A novel add-on hardware hat that provides a programmable and stable output voltage and a very accurate current measuring circuit to support accurate emulation of the complete EH system.
   - Programmable and stable output voltage between 1.2 V and 3.6 V.
   - Current measurement circuit capable of handling currents from $1\,\mu\mathrm{A}$ to $0.6\,\mathrm{A}$.

This work is organized as follows. Section II compares the proposed emulation platform with the state-of-the-art. In Section III, the concept of EH is discussed, with insights into the key components of the generic EH system. The hardware and software design of the emulation platform are outlined in Section IV. Section V evaluates the hardware system and validates the software models. The full potential of the proposed emulation platform is showcased in Section VI, whereas conclusions are presented in Section VII.

II. Related work

In recent research on EH frameworks and emulation platforms, several useful tools have been developed to simulate and test EH scenarios, particularly in the context of WSNs and other low-power applications. These platforms aim to replicate real-world scenarios to evaluate and optimize EH systems. An overview of these platforms is given in Table I.

In [4], a generic energy-harvesting framework is designed to assess the reliability of a carrier-sense multiple access with collision avoidance (CSMA/CA) scheme in emerging large-scale energy harvesting electronic-shelf label (EHESL) systems. Therefore, a real-life testbed with an environment emulator based on the TMote Sky, is proposed. The system emulates a PV cell and a capacitor, which is simulated based on the law of Coulomb, but it does not consider leakage currents and diffusion currents. Leakage current refers to the slow, continuous discharge of stored energy, while diffusion current results from the redistribution of charge within the

TABLE I
Overview of existing emulation platforms.

Emulation Platform	Energy Source			Power Management System			Supercapacitor			
	Captured I-V curves	Simulated		Buck-Boost Converter	MPPT[1]	LDO[2]	Physical	Simulated		
		Solar	RF					Law of Coulomb	Leakage Current	Diffusion Current
EE[3] [4]	-	✓	-	-	-	-	-	✓	-	-
SunaPlayer [5]	✓	-	-	-	-	-	-	-	-	-
Ekho [6]–[8]	✓	-	-	-	-	-	✓	-	-	-
Ripeto [9]	✓	-	-	-	-	-	✓	-	-	-
Shepherd [10]	✓	-	-	Physical[4]	✓	-	✓	-	-	-
DIPS [11]	✓	-	-	✓	-	-	-	✓	✓	-
BPMx [12]	-	-	-	Physical[4]	-	Physical[4]	✓	-	-	-
PLEASE	✓	✓	✓	✓	✓	✓	**-**	✓	✓	✓

[1] MPPT = maximum power point tracking,
[2] LDO = low-dropout regulator,
[3] EE = environment emulator,
[4] Physical = soldered on the platform.

electrolyte, both leading to gradual loss of energy. The emulator has a nominal current resolution of 17 µA and a maximum current load of 70 mA, limiting its applicability to modern low-power sensor applications. Additionally, the conversion stage between the energy harvester and the storage element is not discussed.

Another emulation platform that focuses on solar energy harvesting is the SunaPlayer, presented in [5]. This solar emulation platform supports a wide operating current range from 430 µA to 1.89 A and a voltage range from 0.02 V to 9.8 V, making it versatile for various applications. However, detailed information on the accuracy of the platform and emulation of the power management system or supercapacitor are not provided.

The emulation platform Ekho consists of a field-programmable gate array (FPGA)-based tool capable of recording energy harvesting conditions and accurately recreating those conditions in a lab environment [6]–[8]. Ekho has an accuracy of 77.4 µA for solar and 15 µA for kinetic environments, and can emulate radio-frequency (RF) energy harvesting conditions. One of Ekho's drawbacks is that the supercapacitor is not emulated and a physical storage element is therefore required. In addition, Ekho requires previously generated I-V curves, which can be time-consuming to import when iterating through different energy harvesters and capacitors. The PMU is not emulated either, and the platform does not support a simulation model for a supercapacitor, in contrast to the proposed emulation platform in this paper.

Ripeto [9], another FPGA-based emulation platform, improves upon Ekho by offering more memory storage for I-V curves and an embedded digital logic analyzer. Where Ekho is able to record and save I-V curves with a 64-points resolution, Ripeto can save up to 2048 high resolution I-V curves with 4096 data points each. Ripeto focuses only on solar EH scenarios and achieves a mean error of just 0.56%, indicating its high precision. However, it does not provide a PMU model and requires a physical storage element.

Shepherd, proposed in [10], provides synchronized recording and emulation of multiple energy harvesters, offering insights into the spatio-temporal energy environment. It relies on a converter-based architecture with a physical DC/DC converter between the energy harvester and the supercapacitor, enabling operation at the MPP. Shepherd records energy traces with a resolution of 3 µA and 50 µV at a rate of 100 kHz, replaying them with a mean error below 0.1%. The platform can emulate multiple energy harvesters, but requires pre-captured I-V curves, which can be time-consuming to import when iterating through different harvesters.

In [11], a hardware debugger capable of emulating any power scenario to the DUT is proposed. This system, called Debugger for Intermittently-Powered Systems (DIPS), utilizes prerecorded I-V curves and emulates the boost converter and the supercapacitor, including leakage current in its model but not diffusion current. In addition, it does not include an advanced PMU model with a maximum power point tracking (MPPT) algorithm. Built around the GNU debugger (GDB), DIPS allows for pausing the emulation and program execution, making it a powerful tool for debugging and testing EH systems.

In [12], an extension board is proposed with a fully-configurable PMU with user-defined voltage thresholds, supply voltage in the range [1.8-3.3] V, and the ability to fully disconnect certain subsystems. Moreover, the extension board integrates a real LDO, the TPS62643, and the possibility to solder two supercapacitors, one SMD and one through-hole. However, the platform only supports the use of real components, which limits its flexibility and adaptability for different EH applications.

While existing emulation platforms offer useful features, none achieves the full integration of critical capabilities required for modern EH system design. Specifically, they lack realistic digital-twin models for harvesters and power management units, they do not support advanced supercapacitor modeling with diffusion characteristics, and they often omit high-resolution current measurement. In contrast, the proposed emulation platform uniquely combines accurate digital-twin-based emulation—including indoor/outdoor PV and RF EH, and detailed supercapacitor behavior—with a custom hardware hat for precise voltage control and microamp-level current sensing, all validated through real-world IoT applications.

III. Energy Harvesting

This section provides an overview of EH technologies, including its significance for IoT and other applications, the fundamental architecture of an EH system, common energy sources, the energy conversion stage, and various storage elements used to retain harvested energy.

Replacing batteries with EH technologies offers notable benefits across the environmental, climatic, and economic dimensions. From a climate perspective, we have made a comparison between the input-output global warming potential (GWP) of an IoT device powered by an EH system consisting of a 0.5 Wp (Watt peak) solar cell combined with a 1 mF electrolytic capacitor, versus a device powered by a 2000 mAh lithium battery. During production, the EH-enabled device has a GWP of 254 g CO_2 equivalent (CO_2-eq), versus a GWP of 488 g CO_2-eq for the battery powered device, based on data obtained by the same methodological framework [13]–[15]. This highlights that the device using a capacitor and a solar cell has the most favorable impact on GWP during manufacturing. Furthermore, in locations such as Belgium, at a moderate longitude of about 50° N, the 0.5 Wp solar panel could annually save 220 g of CO_2 compared to a system using electricity generated from natural gas (490 g CO_2-eq/kWh).

Environmentally, battery-powered IoT devices that exploit disposable batteries generate more waste compared to those using EH systems. For example, Samsung has introduced a remote control powered by energy harvested from indoor and outdoor light, as well as Wi-Fi signals. They claim that this technology could prevent 200 million batteries from ending up in landfills over the next seven years [16]. These landfills significantly impact the environment, particularly due to fires frequently caused by discarded batteries [17]. Studies indicate that there may also be short-term increases in the concentration of heavy metals [18] in water bodies near burning sites. Solar

cells and lithium batteries have a low recycling rate, but efforts are being made to improve recycling technologies. Conversely, aluminum, used in capacitors, has one of the highest recycling rates compared to other materials [19].

Economically, although EH eliminates the cost of battery replacements, the initial investment of incorporating EH technologies may be higher, particularly when using a supercapacitor as a storage device. To tackle this trade-off, product designers need to evaluate the long-term benefits against the upfront costs, which are both very application-specific.

A. Energy Harvesting Architecture

Fig. 1 shows the building blocks of a typical EH system interacting with each other. An energy harvester generates electrical power from its environment. This power is transferred by the PMU to the storage element and the IoT device. When the device consumes more power than the harvester can deliver, the PMU will draw extra power from the storage element. In the following subsections, an overview of different energy harvesting sources is given, followed by a discussion of the energy conversion stage and lastly the storage element.

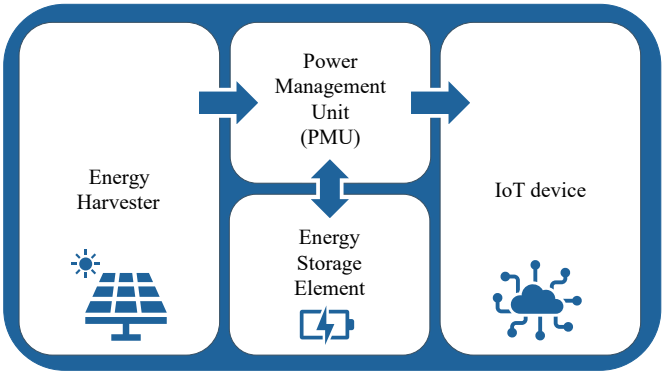

Fig. 1. Typical composition of an IoT device relying on energy harvesting.

B. Overview of Energy Harvesting Sources

Ambient energy sources in the environment are highly variable, posing challenges in designing a functional and reliable device solely depending on these sources [20]. When developing an EH system, the primary consideration is whether the energy source is controllable. If controllable, it becomes feasible to supply the device with energy when needed. Mechanical energy, typically generated by human activity or human-operated machinery, is controllable, similar to RF energy and indoor lighting. In contrast, solar and wind energy are naturally occurring phenomena that are non-controllable in general. For non-controllable energy sources, predictability becomes a key consideration. When predictable, a device's energy consumption can be aligned with the anticipated energy availability. Table II provides an overview of various energy sources, including an estimate of power production to provide insight into their respective power densities.

TABLE II
CHARACTERISTICS OF DIFFERENT ENERGY SOURCES.

Energy Source	Controllable	Predictable	Approximate Power Production
Solar	×	✓	100 mW/cm^2 [21]
Wind	×	✓	0.59 mW/cm^3 [22]
Kinetic	✓	-	100 mW - 250 mW (80 km/h) [3]
Vibration	✓	-	0.08 mW - 0.15 mW (50 Hz) [3]
RF	✓	-	1 µW/cm^2 (900 MHz) [21]
Ambient Light	✓	-	0.1 mW/cm^2 [21]

C. Energy Conversion

Energy conversion from the harvester to the supercapacitor is achieved using a charging circuit, whereof two different types exists [10]. The first, a converterless approach relies on a diode that permits current flow only when the harvester voltage exceeds the capacitor voltage ($V_{storage}$) plus the threshold voltage of the diode (V_{diode}). Combining the harvester's I-V curve with the operating voltage ($V_{storage} + V_{diode}$) yields the output current. However, since $V_{storage}$ is variable, this operating point will vary during the process and fluctuate around the MPP.

The second type of circuit is a converter-based circuit. A boost converter is placed between the energy harvester and the storage element. This boost converter aims to operate the harvester at its MPP, typically by selecting an operating point at a predefined fraction of the open-circuit voltage (V_{oc}), e.g. $0.8V_{oc}$. The boost converter increases the input voltage ($0.8V_{oc}$) to the voltage of the storage element. The supercapacitor is then charged with a current equal to

$$I_{charge} = \frac{\mu V_{harvester} I_{harvester}}{V_{storage}}, \tag{1}$$

with μ the DC-DC converter losses, typically ranging from 50% to 95%, depending on the input voltage ($V_{harvester}$) and the input current ($I_{harvester}$).

D. Storage Element

The choice of storage elements in EH systems depends on several factors such as energy density, life cycle, form factor, and application requirements. Supercapacitors are commonly used in energy harvesting applications, typically ranging from millifarads (mF) to farads (F) and they are mostly electric double-layer capacitors (EDLC). Supercapacitors are characterized by a high power density but a low energy density. They can discharge their energy very quickly, causing a rapid decrease in terminal voltage. The voltage across the capacitor must not exceed a specified limit, otherwise there will be breakdown of the separating structure inside the capacitor. Generally, supercapacitors are relatively expensive, which limits their use to niche applications. However, a supercapacitor is more eco-friendly than a battery. It is more resistant to

environmental changes, exhibits a longer lifetime and the price per farad is decreasing (Table III). This makes supercapacitors a promising technology for future applications.

TABLE III
COMPARISON BETWEEN BATTERY AND SUPERCAPACITOR.

Property	Battery	Supercapacitor
Power Density (W/L)	$10^3 - 3 \cdot 10^3$	< 500
Energy Density (Wh/L)	50 - 300	0.5 - 5
Lifetime (cycles)	200 - 1000	$10^6 - 10^8$
(Dis-)charge Rate	30 - 600 min	ms - min
Temperature (°C)	0 - 45	-45 - 45

While this study focuses on the design of battery-less sensor systems, the choice of the storage element or energy buffer depends on the specific application requirements. Supercapacitors are well suited for devices in hard-to-reach places or massive-scale sensor networks, where maintenance is impractical. However, applications that require more stable voltages and lower leakage currents might still benefit from batteries or a hybrid configuration, offering both performance and long-term autonomy.

IV. PLEASE

This section introduces PLEASE, our novel open-source emulation platform for the development of sustainable battery-less sensor systems. An overview of the key requirements is provided, followed by a high-level description of the system architecture. Next, the custom-designed analog front-end is discussed, focusing both on the power supply and the power consumption measurement. Lastly, the custom-developed software, running on the RPI, is explained.

A. Key Requirements

For the energy harvesters, the software should include models for both indoor and outdoor PV cells. It should be possible to emulate the harvester based on basic properties found in the datasheet, eliminating the need to purchase and test the harvester itself. Consequently, it should be feasible to iterate through various setups by adjusting the fundamental parameters. In addition, it should be possible to emulate rectifiers and rectenna systems based on measured or simulated I-V curves, which can be imported into the emulation platform. The PMU simulation model should account for conversion losses, which significantly impact the overall efficiency of the system. The supercapacitor model includes both leakage currents and absorption currents, as these affect the voltage across the capacitor even when the load is disconnected. To accommodate additional testing, a trace of the light intensity is used to define a dynamic environment, which should be coupled to the solar model. This allows the estimation of the performance and energy margins under varying dynamic conditions.

Emulating the state of the storage element requires knowledge of the power consumption of the DUT. Thus, the hardware must include a circuit capable of measuring the power consumption of the DUT. The accuracy should preferably be in the same order as the resolution to accurately measure the power consumption in low-power modes. Such as the deep-sleep mode, where a DUT spends most of its time. The output of the simulated EH system should provide a stable output voltage between 1.2 V and 3.6 V. This voltage should be made available to the DUT through a programmable power supply.

B. System Architecture

Fig. 2 provides a graphical representation of the system under study, detailing its building blocks. The system starts by emulating the harvested energy, incorporating solar, indoor light and RF. It employs a custom-developed algorithm, which is further discussed in section IV-D, to convert datasheet parameters into parameters for the one-diode model. Once this

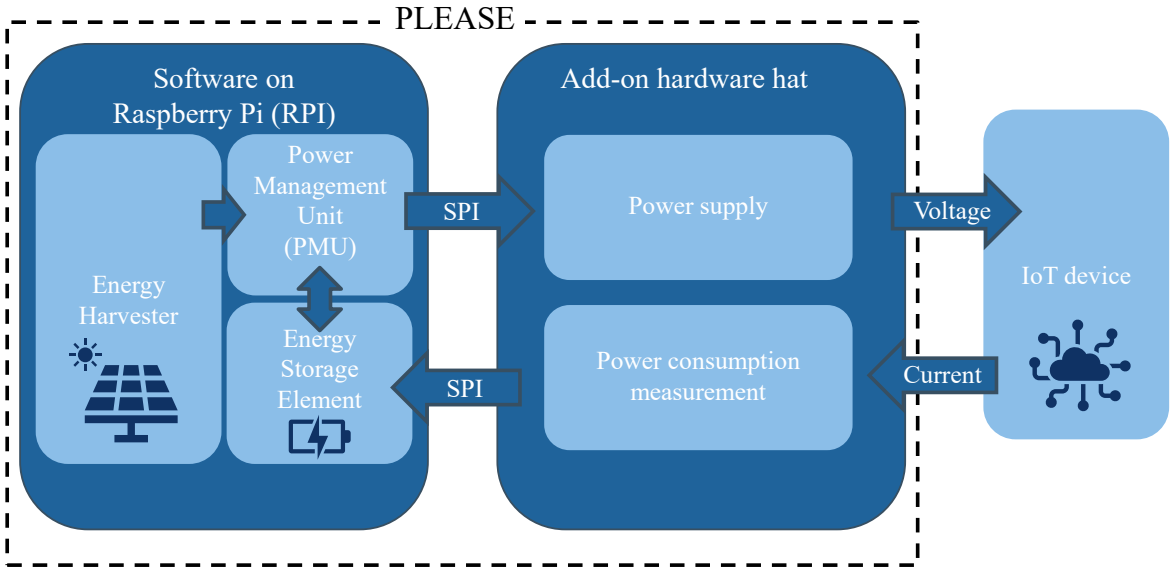

Fig. 2. System architecture of PLEASE, with the software deployed on a Raspberry Pi (RPI) and an add-on hardware hat with a power supply and a power consumption measurement circuit.

model is established, it can be interpolated for varying light intensities, which is crucial for coupling the light trace to the solar model. The output of the *Energy Harvester* block is an appropriate I-V curve that serves as input to the *PMU*. This PMU selects an operating point on this I-V curve and directs this power to the *Energy Storage Element* block, accounting for corresponding conversion losses. When the storage element accumulates sufficient charge, the PMU communicates with the add-on hardware hat to activate the *Power Supply* block via the Serial Peripheral Interface (SPI), enabling the start-up of the DUT. The *Power Consumption Measurement* block measures the current consumption of the IoT device and transmits these data via the SPI to the RPI. Finally, the voltage drop over the supercapacitor is calculated using the current measurement value, along with the emulated leakage currents and absorption currents.

C. Add-on Hardware Hat

The first subsystem of the add-on hardware hat, depicted in the block diagram in Fig. 3 and in the schematic layout in Fig. 4, is the *Power Supply* circuit. This circuit includes a digital-to-analog converter (DAC), used to transform the digital simulated LDO output to the correct voltage. The output voltage of the DAC is buffered by an operational amplifier (OpAmp), labeled Buffer in Fig. 3, followed by a bipolar junction transistor (BJT) in a common collector configuration. The supplied voltage is made available at the header pins for DUT connection.

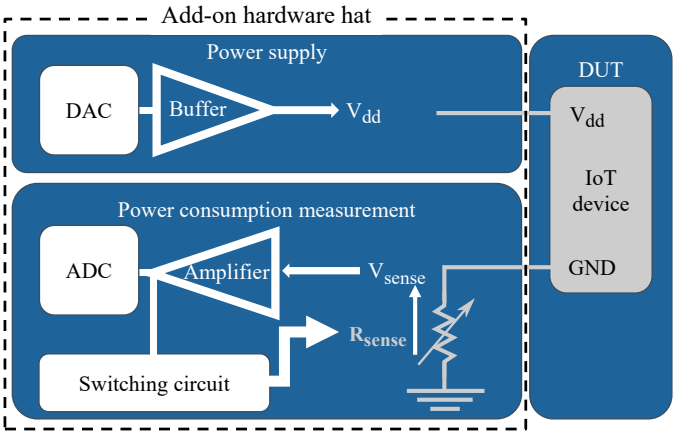

Fig. 3. High-level architecture of the add-on hardware hat, with the power supply circuit and the power consumption measurement circuit.

The second subsystem of the add-on hardware hat is the *Power Consumption Measurement* circuit. The current consumed by the DUT is measured via the corresponding voltage drop across a series resistor R_{sense}. Due to the wide range of current values (1 µA - 600 mA), applying a fixed amplification would result in either large voltages or limited resolution. Therefore, a variable resistor is implemented by switching between these resistors in parallel, thereby decreasing the equivalent series resistance when the voltage drop becomes too high. This approach acts as a variable amplification factor to prevent saturation.

This concept requires an analog switching circuit based on Schmitt-triggers to switch between resistors. There are four stages in total, each with a different equivalent resistance R_{sense}, as shown in Table IV. Additionally, a fixed amplification factor of 42 is applied to amplify the small voltage drop across the equivalent series resistor, resulting in the amplified voltage V_{ampl} without offset, as indicated in Table IV. To prevent the OpAmp from saturating at a voltage of 5 V, an offset of -3 V is introduced, increasing the dynamic range of the amplifier. Finally, the amplified voltage is converted using a 12-bit analog-to-digital converter (ADC) and sent to the RPI.

TABLE IV
VARIABLE R_{SENSE}, V_{SENSE} AND RANGE OF V_{AMPL} WITH AND WITHOUT OFFSET FOR EVERY CURRENT STAGE.

Current [mA] **Mode**	**0 - 0.35** **Deep Sleep**	**0.35 - 3.5** **Low Power**	**3.5 - 46** **Active**	**46 - 600** **Tx**
R_{sense} [Ω]	470	43	3.6	0.25
$V_{sense}[mV]$	0 - 165	15 - 165	12 - 165	11 - 150
$V_{ampl}[V]$, no offset	0 - 6.9	0.6 - 6.9	0.5 - 6.9	0.5 - 6.3
$V_{ampl}[V]$, offset -3 V	-3 - 3.9	-2.4 - 3.9	-2.5 - 3.9	-2.5 - 3.3

Both subsystems, along with their peripherals connected to the RPI, are carefully placed on a printed circuit board (PCB), as depicted in Fig. 4. The power electronics, which emit the highest EM-radiation due to internal switching, are isolated by vias and placed sufficiently far from the sensitive electronics. The DAC and ADC communicate with the RPI through the SPI. To optimize this high-frequency communication, the traces are kept as short as possible. The PCB is designed as a two-layered structure, with the backside plane maximally utilized as a reference plane. The traces carrying the supply voltage are widened to minimize the resistive power losses.

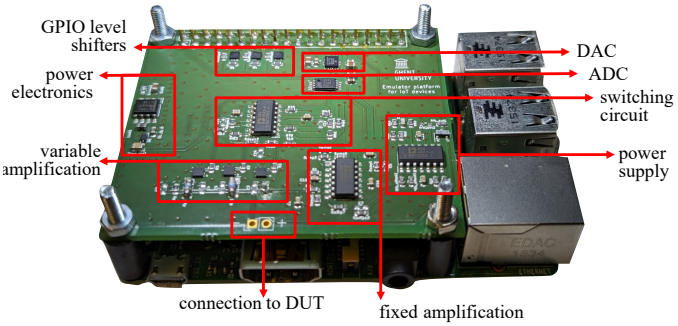

Fig. 4. Schematic layout of the add-on hardware hat, with all the components annotated.

D. Software

1) Solar and Indoor Light EH Emulation: The one-diode model is the most widely utilized and fundamental electrical equivalent circuit for representing the behavior of a solar cell, using only basic electronic components, as illustrated in Fig. 5. This model not only offers simplicity but also provides an accurate representation of real solar cell performance, making it highly effective for this application.

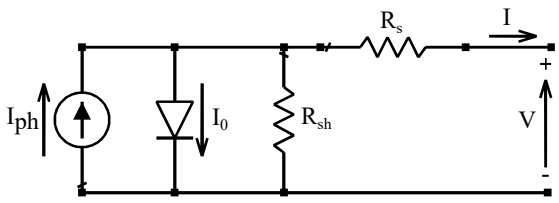

Fig. 5. One diode model of a solar cell, with the photo current (I_{ph}), diode current (I_{o}), shunt resistance (R_{sh}), and series resistance (R_{s}).

The following custom algorithm has been developed to estimate the parameters of the one-diode model using only three known points from the I-V curve: the open-circuit voltage, the short-circuit current, and the MPP. The algorithm performs a sweep over two non-linear parameters, being the ideality factor a and the series resistance R_s. Based on these three known points, the remaining parameters of the one-diode model are calculated. The algorithm selects the combination (a,R_s) that generates the flattest power curve at the MPP. Once these parameters are determined, the model can predict the behavior of the solar cell under different lighting conditions through interpolation, allowing for a flexible and efficient modeling approach using only datasheet information.

This method is based on (2), which describes the relationship between the output current (I) and voltage (V) of the solar cell:

$$I = I_{\mathrm{ph}} - I_{\mathrm{o}} \left[\mathrm{e}^{\frac{V+IR_{\mathrm{s}}}{a}} - 1 \right] - \frac{V + IR_{\mathrm{s}}}{R_{\mathrm{sh}}}, \tag{2}$$

with I_{ph} the photo current, I_{o} the diode current, a the ideality factor, R_{s} the series resistance and R_{sh} the shunt resistance. This relationship gives rise to the typical I-V curve of a solar cell. Although this method is less accurate than approaches that rely on more data points, it offers a simple and practical solution for modeling solar cells in various environments based on limited information [23]. In addition, the emulation platform offers the possibility to import more detailed I-V curves when increased accuracy is required.

2) Radio-Frequency (RF) EH Emulation: To replicate RF EH, we must emulate the behavior of a rectifier or even a complete rectenna system. Therefore, the platform allows the designer to import a set of I-V curves. These curves can be derived either from direct measurements with a source measure unit (SMU) or through simulation frameworks such as Keysight PathWave Advanced Design System (ADS). Since a typical rectenna system generates a distinct I-V curve for each input power level, it is necessary to import a complete set of relevant I-V curves corresponding to input power levels observed in an application. This enables designers to accurately emulate the behavior of a rectenna system in environments where the RF power at the input of the rectenna can be estimated.

3) Power Management Unit (PMU) Emulation: The efficiency of the LDO is primarily determined by resistive losses, meaning that the power extracted from the supercapacitor is the product of the voltage across the supercapacitor and the current drawn by the DUT.

The efficiency of the boost converter is more dynamic, depending on the input voltage (V_{in}), input current (I_{in}) and output voltage (V_{out}). To determine its boost conversion efficiency (μ) at a specific operating point ($\mu(V_{\mathrm{in}}, I_{\mathrm{in}}, V_{\mathrm{out}})$), a 3D interpolation between the known efficiency curves is required. In practice, this interpolation process is computationally intensive. To reduce CPU time, the boost conversion efficiency computation must be simplified. Analysis of previously published boost conversion efficiency curves [24] shows that variations in output voltage have less impact on efficiency than variations in input voltage or current, particularly when the input voltage is below the output voltage. Furthermore, these data indicate that when the input voltage exceeds the output voltage, the boost conversion efficiency reduces to approximately 80% [24]. To model these simplifications, the following formula is used to calculate the power entering the storage element ($P_{storage,in}$):

$$P_{storage,in} = \begin{cases} \mu(V_{in}, I_{in}) V_{in} I_{in}, & \text{if } V_{in} < V_{out} \\ 0.8 \cdot V_{in} I_{in}, & \text{if } V_{in} > V_{out}. \end{cases} \tag{3}$$

This approach reduces the interpolation to a 2D space, thereby saving CPU time. If the operating point of the harvester is known in advance, a designer can opt to specify a fixed efficiency.

4) Supercapacitor Emulation: To accurately emulate a supercapacitor, it is crucial to account for the effects of leakage current, absorption current, and internal resistance. This is achieved by relying on the equivalent schematic shown in Fig. 6. The equivalent series resistance (ESR) represents the power losses due to internal resistance. The shunt resistor (R_{leak}) models the leakage current of the primary capacitance (referred to as the effective capacitance C_{eff}). The RC circuit in parallel with this effective capacitance models the time-varying diffusion current. It is important to note that this model approximates the diffusion current by a first-order model with an exponential behavior ($\tau = R_{diff} C_{diff}$), which provides a good approximation of the actual diffusion current dynamics. In reality, this behavior is a superposition of multiple RC circuits with different time constants [25].

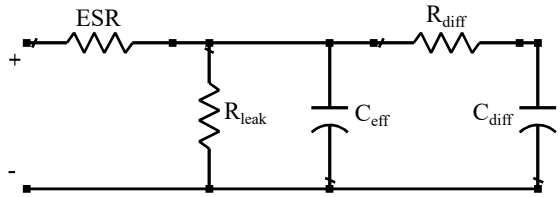

Fig. 6. Supercapacitor equivalent schematic.

In addition, the modular design of the environment emulator software makes it possible to add more advanced models of batteries, such as the battery dynamic model proposed in [26]. This widely adopted model integrates accurate charge and discharge models for different types of battery technologies.

V. Evaluation

We now validate the proposed open-source emulation platform. First, the accuracy of the power measurement circuit on

the add-on hardware hat is discussed. Second, the simulation models for the solar and RF energy harvesters are verified through measurements. Next, the PMU functionality is validated with different measurements. Lastly, the accuracy of the supercapacitor model is measured and compared with a real supercapacitor.

A. Power Consumption Measurement

The *power consumption measurement* subsystem, located on the add-on hardware hat, was validated first. Fig. 7 shows the mapping of the input current to the output voltage, which is shown in blue. The discontinuities in the output voltage are the result of switching in order to include additional resistors in parallel. This switching and variable amplification ensure that the output voltage remains within the [-5 V; 5 V] range for all currents. The current values activating the p-channel metal-oxide semiconductor (PMOS) transistors, are visible through the discontinuities of the green, red and purple curves. These values match closely those listed in Table IV. The emulation platform will reversely map the output voltage to the input current, utilizing the V_{SWi} signals to eliminate the ambiguity of the variable amplification and determine the correct current.

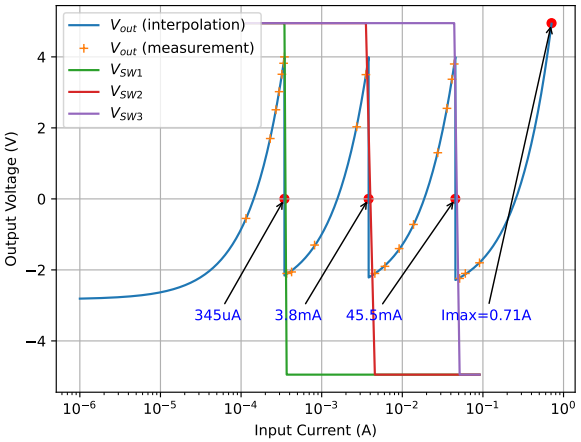

Fig. 7. Current sensing outputs with $V_{offset} = -2.8\ V$.

When the reverse mapping to the input current is performed using the nominal resistance values (see Table IV) and the theoretical static amplification, the measured value deviates by 0.31% from the actual current value in the lowest current range. This deviation corresponds to a guaranteed accuracy of 1.1 µA. When a calibration procedure is executed before measurements, this accuracy can be improved to 0.17%, corresponding to an absolute error of 0.6 µA for an input current up to 350 µA. This means that the deep-sleep power consumption can be measured with an accuracy below 1 µA, meeting the requirements. The calibration measures the effective offset and effective amplification factors. For each stage, the accuracy range and error are provided in Table V.

B. Solar EH

The outdoor solar cell is measured in a setup with a variable artificial light source, characterized by a broad spectrum similar to that of the sun. The indoor solar cell was measured under two realistic indoor lighting setups. A lux meter was used to quantitatively compare the two lighting conditions. These lux values were used in the model, since a pyranometer, an instrument to measure solar irradiance, was not available. This does not affect the results because the relative change in irradiance is equal to the relative change in illuminance given that the light spectrum remains unchanged.

TABLE V
ACCURACY OF THE CURRENT MEASUREMENT SYSTEM.

	Accuracy			
	Before Calibration		After Calibration	
Stage	Error (%)	Range (µA)	Error (%)	Range (µA)
0 µA - 350 µA	0.31	0 - 1.1	0.17	0 - 0.6
350 µA - 4 mA	3.14	11 - 250	0.07	0.25 - 3
4 mA - 48 mA	1.67	67 - 630	0.11	4.4 - 50
48 mA - 0.71 A	6.23	3000 - 45000	2.52	1200 - 18000

The I-V curves of the measurements and the one-diode model, with parameters listed in Table VI, align very well, as seen in Fig. 8. The algorithm that estimates the reference I-V curve (blue) is highly accurate. The root mean square error (RMSE) between the simulation and measurement equals 0.6 µA (0.5 of $\%I_{\mathrm{sc}}$) for the indoor cell and 4.6 µA (0.6 of $\%I_{\mathrm{sc}}$) for the outdoor cell. Another advantage of this algorithm is that the MPPs of both the measurement and simulation coincide. The interpolation for different lighting conditions generates an I-V curve (orange) that falls within the measured curve region. Although the open-circuit voltage of the indoor panel is slightly different, the maximum power value deviates by less than 7%. For the outdoor solar cell in low light conditions, the maximum power deviates by less than 4%.

TABLE VI
ONE-DIODE MODEL PARAMETER RESULTING FROM THE CUSTOM-DEVELOPED ALGORITHM, DISCUSSED IN SECTION IV-D.

Parameter	Indoor cell [27]	Outdoor cell [28]
Rs	0.1 Ω	3 Ω
Rsh	340 kΩ	150 kΩ
I_0	20 nA	0.62 µA
I_{ph}	0.11 mA	0.82 mA
a	0.55	0.68

C. RF EH

The rectifier of the rectenna was measured using an SMU for various input powers, provided by a Keysight N5247A PNA-X Microwave Network Analyzer configured in continuous-wave (CW) mode. The I-V and power-voltage (P-V) curves resulting from the measurements, as well as those generated by the ADS simulation model, are shown in Fig. 9. While the measurement results are slightly lower, they remain reasonably accurate, as the MPPs of both the measured and simulated curves are nearly identical.

D. Power Management Unit

Next, the AEM10941 PMU by e-peas [24] is emulated: its characteristics will be simulated in software, and the output

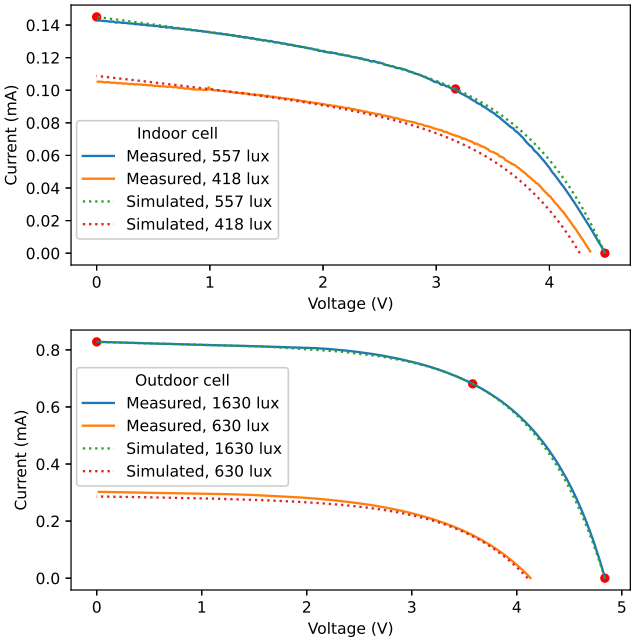

Fig. 8. Validation of the solar EH model: I-V curve of the TDK BCS4430B6 indoor cell (top) and Seeed studio 0.5W outdoor cell (bottom), with red dots marking the short-circuit current (I_{sc}) on the left, the maximum power point (MPP) in the middle, and the open-circuit voltage (V_{oc}) on the right.

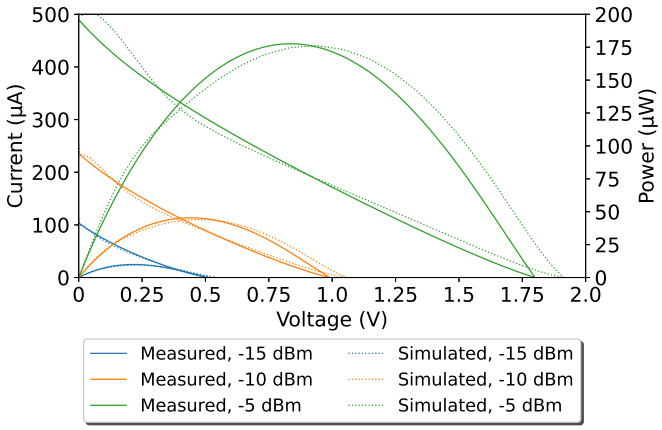

Fig. 9. Measured and simulated IV- and PV-curves of the rectifier.

of the PMU, a stable voltage for the load, will be physically available on the add-on hardware hat. The emulation of a PMU consists of three components, the boost converter, the control system, and the LDO. For simulating the boost converter, conversion efficiency curves from a datasheet are imported using a plot digitizer. The control system uses three parameters set by the designer: V_{ovdis} as the voltage limit when the LDO is disabled, V_{chrdy} as the minimum voltage to enable the LDO and V_{ovch} as the maximum voltage on the storage element before disabling the boost converter. The LDO also relies on a conversion efficiency curve based on the desired output voltage. This curve can be imported from the datasheet.

To test the emulation of a PMU, a simple setup is analyzed using actual hardware and then reproduced by the emulation platform. Fig. 10 shows the temporal behavior of the voltage across the supercapacitor in a simple EH setup. The blue curves are the result of a setup based on a 0.5 V fixed input voltage, while the green curves depend on a 3 V fixed input voltage, both setups using a 10 mA input current. The PMU's control parameters are indicated in red, with V_{ovdis} = 3.60 V, V_{chrdy} = 3.92 V and V_{ovch} = 4.50 V. The dotted lines represent the results obtained by the PLEASE emulator with an identical setup in software. A notable difference between emulation and measurement is the sawtooth-wave-like behavior at the end of the green curve. This non-ideality is not described in the datasheet but is likely due to built-in hysteresis to prevent the source from switching on and off at a high rate.

In addition to validating the control parameters, the results in Fig. 10 demonstrate that the emulation platform accurately models the conversion efficiency. When the input conditions of the PMU are changed, the emulation platform accurately includes the conversion efficiency losses in the emulation.

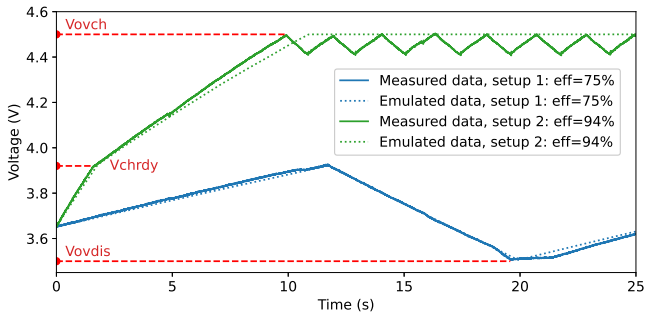

Fig. 10. Measurement and emulation of the PMU "AEM10941" with the "BestCap BZ015A503Z_B" supercapacitor of 50 mF, fixed load of 1.2 kΩ, fixed input current 10 mA, and variable input voltage resulting in different efficiencies.

E. Supercapacitor

The parameters of the supercapacitor model are established by fitting the effective capacitance to a constant current charging curve and fitting the other parameters to a self-discharge curve of 10 minutes with a holding voltage of 5.5 V and a holding time of 10 seconds. These parameters are listed in Table VII for the BestCap BZ015A503Z_B [29].

TABLE VII
PARAMETERS FOR "BESTCAP BZ015A503Z_B" FITTED TO THE SELF DISCHARGE CURVE OF V_{CHARGE} = 5.5 V AND t_{HOLD} = 10 S.

Parameter	Value	Parameter	Value
C_{nom}	50 mF	C_{eff}	36 mF
ESR	0.15 Ω	R_{leak}	1491 kΩ
C_{diff}	4.8 mF	R_{diff}	45 kΩ

The model provides highly accurate results for this reference self-discharge condition, as shown by the blue curves in Fig. 11. Other self-discharge curves exhibit minor deviations between simulations and measurements. The orange curves reflect the same behavior but with slightly different time constants, while the green curves display the same quasi-linear behavior but with slightly different leakage currents. These

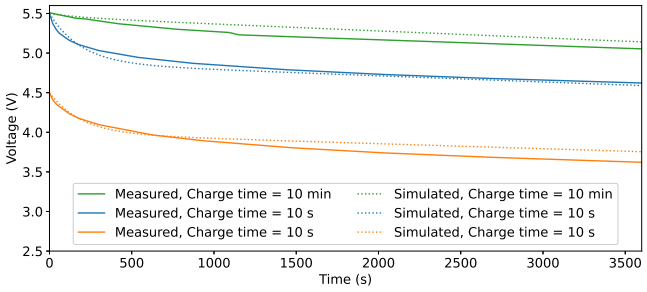

Fig. 11. Validation of the supercapacitor model for the BestCap BZ015A503Z_B, parameters fitted to blue curve (V_{charge} = 5.5 V and t_{hold} = 10 s).

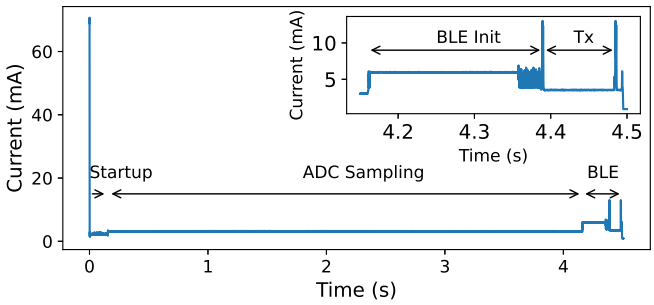

Fig. 12. Current consumption profile of the heart rate monitor application when powered by a 3.3 V power supply.

discrepancies can be attributed to the first-order approximation used in the model.

Extending the model to a continuous distribution of RC constants would be overly complex and not user-friendly. Hence, the first-order approximation will continue to be employed, with the discharge curve being fitted accordingly. Additionally, the diffusion characteristic may be neglected, and a simpler supercapacitor model based on datasheet parameters may be utilized.

VI. Validation

The operation of the proposed emulation platform is validated using two relevant example applications: a heart-rate monitor powered by indoor light EH and a temperature sensor powered by RF EH.

A. Heart-Rate Monitor based on Indoor Light EH

The first application is a Bluetooth enabled heart-rate monitor, powered by indoor light EH. The heart-rate monitor uses a Pulse Sensor [30] in combination with an STM32WB55 ultra-low-power wireless microcontroller unit (MCU) [31]. The Pulse Sensor is a low-cost optical heart-rate sensor, which is connected to one of the ADC pins of the MCU. In EH applications, it is important that the software is optimized for power efficiency. Therefore, this application encapsulates the sensor data into the Bluetooth Low Energy (BLE) advertising packets to minimize the power consumption by the data packets transmission [32]. A BLE receiver is configured in continuous listening mode. It can capture the transmitted advertising packets in real-time by using an infinite scanning loop. The power consumption profile of this heart rate monitor application is depicted in Fig. 12, where every task is annotated on the graph. It was measured with a Power Profiler II Kit by Nordic Semiconductors [33]. The total measured energy of single duty cycle, averaged over 10 measurements, equals 46.83 mJ for a supply voltage of 3.3 V and 39.18 mJ for a supply voltage of 3 V, which is the minimal supply voltage for the Pulse Sensor [30].

In a typical operating cycle of the heart-rate monitor, the MCU first boots from scratch, initializes all the required peripherals and configures the system clock. Second, the ADC is enabled and the MCU reads a sample from the Pulse Sensor every 10 ms within a 4 s time period. Next, the heart rate is calculated by comparing the ADC samples to a threshold value and the result is encapsulated in an advertising packet. In a final step, the BLE transceiver is initialized and two advertising packets are transmitted at an output power level of 0 dBm.

The following sections detail the implementation, measurement setup, and optimization strategies for maximizing performance while operating within the constraints of harvested energy.

1) Emulation and Measurement Setup: For this application scenario, different hardware configurations are analyzed using the proposed emulation platform and a realistic measurement setup. The first setup is the actual application, consisting of the Pulse Sensor, connected to the ADC of the MCU, which is powered with the AEM10941 PMU by e-peas [24], in combination with a supercapacitor and the TDK BCS4430B6 indoor light EH [27]. The voltage across the supercapacitor was measured using a Keithley 2450 SourceMeter, which was set to source current in the lowest available range of 10 nA while measuring the voltage [34]. The second setup uses the proposed emulation platform, which replaces the entire EH system, and powers the application via two header pins. Both setups are depicted in Fig. 13.

We first study the hardware in its MPP configuration. The AEM10941 PMU is specifically designed for PV cell harvesting and features different V_{oc} ratios. Second, the supercapacitor configuration is optimized for the total amount of energy required for a single duty cycle. Finally, the optimal configuration for this specific application is discussed.

2) MPP configuration: The MPP is configured based on the simulated I-V curves of the TDK BCS4430B6 indoor light cell. In the process, for the AEM10941, we may set the V_{oc} ratio to 70%, 75%, 85% or 90% [24]. This application is tested for an indoor office environment with a constant illuminance of 500 lux. In Fig. 15, the simulated I-V and P-V curves for this illuminance value is shown with its corresponding MPPs and V_{oc} ratios of 70%, 75%, 85% or 90%. Based on the results in Fig. 15, the MPP of the TDK BCS4430B6 PV cell amounts to 73.79%, which is between the V_{oc} ratios of 70% and 75%.

The emulated and measured voltage across the supercapacitor for a MPP configuration of 70%, 75% and 85% is shown in Fig. 14. The results show that the emulated voltage across the supercapacitor closely matches the measured voltage, indicating the accuracy of the proposed emulation platform.

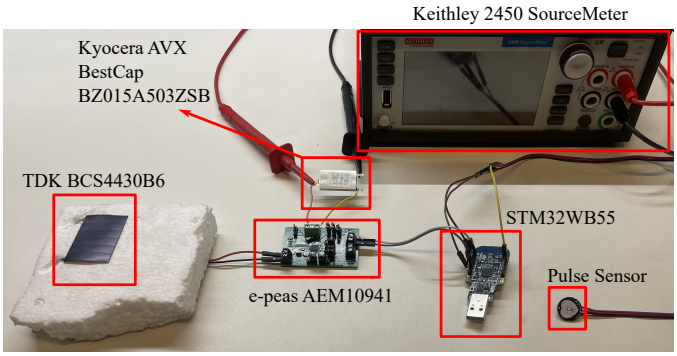

(a)

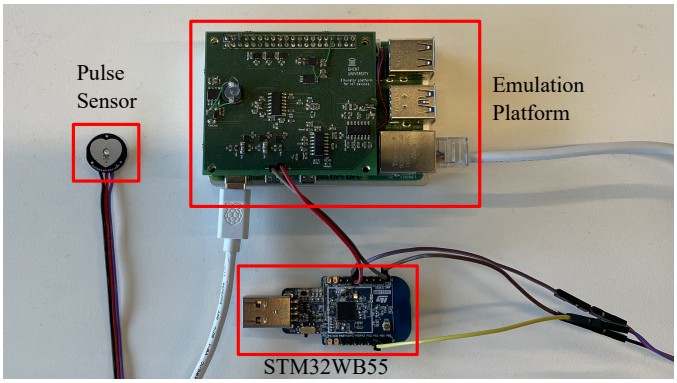

(b)

Fig. 13. Hardware setups for the heart rate monitor application based on RF EH: (a) with the real EH system, (b) with the emulation platform.

3) Size and Configuration of the Supercapacitor: Based on the measured power consumption of a single duty cycle, we determine the minimal size of the supercapacitor via:

$$E = \frac{C \cdot (V_{max}^2 - V_{min}^2)}{2}, \tag{4}$$

with E the energy (J), C the total capacitance (F) of the supercapacitor, V_{max} the maximum voltage (V) the supercapacitor is charged to and V_{min} the minimum voltage (V) the supercapacitor is discharged to. To calculate the minimal capacitance of the supercapacitor, the PMU's control parameters, V_{ovdis}, V_{chrdy} and V_{ovch}, need to be evaluated. The default storage element threshold voltages for a dual-cell supercapacitor are V_{ovdis} = 3.60 V, V_{chrdy} = 3.92 V and V_{ovch} = 4.50 V [24].

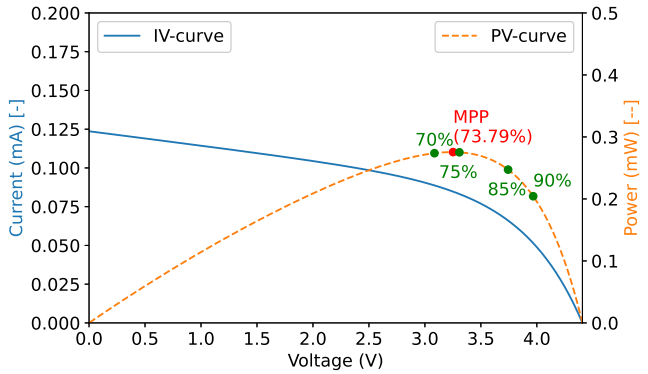

Fig. 15. Simulated I-V curve and P-V curve of the TDK BCS4430B6 indoor light cell for an illuminance value of 475 lux, annotated with its corresponding MPPs.

The maximum settings for an LDO output voltage of 3 V are V_{ovdis} = 3.30 V, V_{chrdy} = 4.45 V and V_{ovch} = 4.50 V, resulting in a minimal total supercapacitor capacitance of 8.79 mF for a total energy of 39.18 mJ, calculated via (4). To provide some flexibility for the configuration, the Kyocera AVX BestCap BZ015A503ZSB, with a nominal voltage of 5.5 V and a total capacitance of 50 mF, was chosen as the primary and only storage element for this application.

By lowering the LDO output voltage from 3.3 V to 3 V, the required energy is reduced, the supercapacitor operates at a lower voltage, and the application's duty cycle increases. Thus, V_{chrdy} can be adjusted to the lowest value that still provides sufficient energy. Using (4), the minimal energy requirement of 39.18 mJ at 3 V results in a theoretical V_{chrdy} = 3.61 V, assuming no losses and V_{ovdis} = 3.3 V, with an effective capacitance of 36 mF (Table VII). The proposed emulation platform enables rapid testing, verification, and efficient emulation of different settings to optimize performance. During this process, a BLE receiver connected to the RPI via a universal asynchronous receiver-transmitter (UART), analyzes the packet update rate of the heart-rate monitor application. Fig. 16 presents two emulation results for different supercapacitor configurations: the first, with V_{chrdy} = 3.77 V, shows a similar packet update rate to the default setting, while the optimized configuration, with V_{chrdy} = 3.67 V, achieves the best update rate.

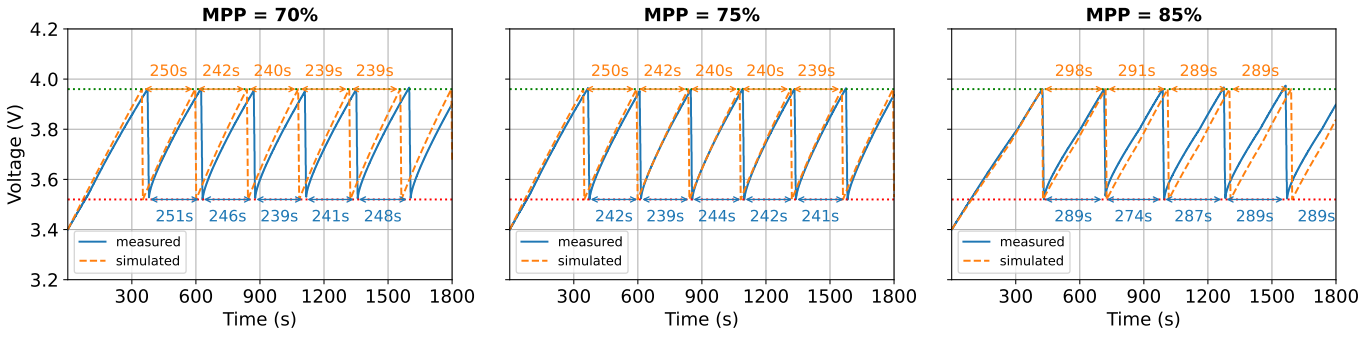

Fig. 14. Emulated and measured voltage across the supercapacitor for a MPP configuration of 70% (left), 75% (middle) and 85% (right).

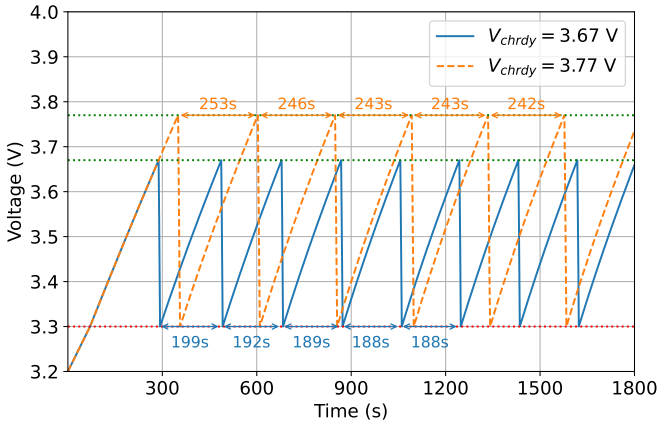

Fig. 16. Emulated voltage across the supercapacitor, as a function of time, for two different supercapacitor configurations with V_{LDO} = 3 V and V_{ovdis} = 3.3 V.

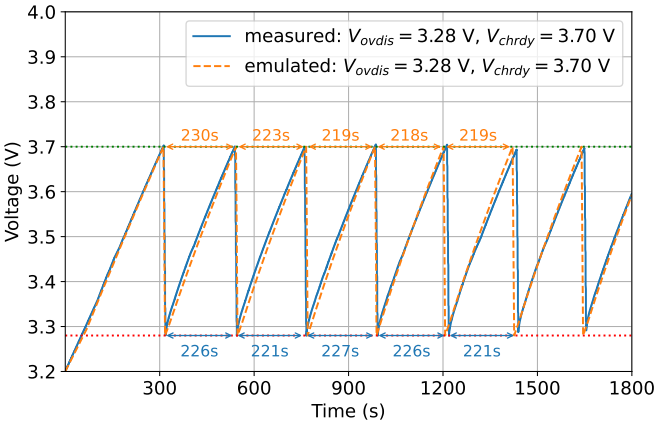

Fig. 17. Emulated and measured voltage across the supercapacitor, as a function of time, for the optimal configuration, showing a very close match between the emulated and experimental results

4) Optimal Configuration: The PMU used in this application, the AEM10941 by e-peas [24], is now configured as closely as possible to the optimal configuration, V_{ovdis} = 3.30 V and V_{chrdy} = 3.67 V, via extra resistors. The ideal and E12 resistor values are shown in Table VIII.

TABLE VIII
OPTIMAL RESISTOR CONFIGURATION FOR THE AEM10941 WITH V_{OVDIS} = 3.30 V AND V_{CHRDY} = 3.67 V [24].

Resistor	Ideal	E12
R_1	1.333 MΩ	1.2 MΩ
R_2	0.302 MΩ	0.33 MΩ
R_3	0.183 MΩ	0.18 MΩ
R_4	4.182 MΩ	3.9 MΩ

Due to the use of these E12 resistors and the tolerance on them, the measured threshold voltages deviate from the ideal configuration: V_{ovdis} = 3.28 V and V_{chrdy} = 3.70 V, which is seen in the measured voltage across the supercapacitor in Fig. 17. Finally, the emulation was updated with these new threshold voltages to show again the accuracy of the proposed emulation platform.

B. Temperature Monitor based on RF EH

The second application is a BLE-enabled temperature sensor, which can be deployed in hard-to-reach locations and is therefore powered via RF EH. This specific representative application uses the same STM32WB55 ultra-low-power wireless MCU as in the first example and its onboard temperature sensor [31]. Similar to the first application, the sensor data are encapsulated into BLE advertising packets to minimize the power consumption of data packet transmission [32]. In addition, unnecessary decoupling capacitors were removed from the STM32WB55 board to reduce the initial current spike. The power consumption profile of this application was again measured with a Power Profiler II Kit. It is depicted in Fig. 18, with every task annotated on the graph. The measured total power of a single duty cycle, averaged over 10 measurements, equals 2 mJ of energy when powered at 1.8 V. Further reduction of the energy consumption may be achieved by modifying the startup cycle and optimizing the embedded software.

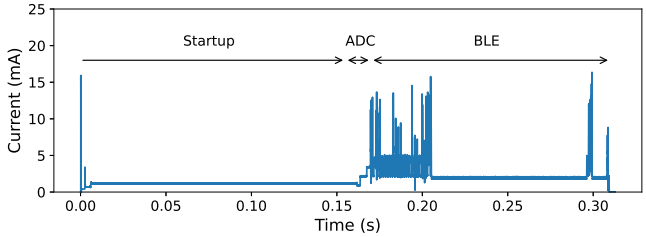

Fig. 18. Current consumption profile of the temperature-monitor application when powered by a 1.8 V power supply.

The following sections detail again the measurement setup, MPPT configuration tuning, and the final optimized system parameters for maximizing performance under RF EH constraints.

1) Emulation and Measurement Setup: For this second application scenario, a different measurement setup is required. The RF EH setup, depicted in Fig. 19, depends on a wireless power transfer (WPT) platform, which is configured to transmit a CW signal at a frequency of 2.45 GHz [35]. This WPT platform is connected via a SubMiniature Version A (SMA) connectorized cable to an air-filled substrate integrated waveguide (AFSIW) cavity-backed slot antenna [36], providing a gain of 6.0 dBi at the center frequency of 2.45 GHz. An identical antenna serves as the receive antenna. This antenna is connected to a carefully optimized rectifier operating at 2.45 GHz [37]. The AEM30940 PMU by e-peas is used in this application, designed to extract power from an ambient RF signal [38]. Again, the Keithley 2450 SourceMeter, configured to provide current in the lowest possible range of 10 nA, is used to measure the voltage over the supercapacitor. Here, the Kyocera AVX BestCap BZ094B153ZSBA1 supercapacitor, with a nominal voltage of 4.5 V and a total capacitance of 15 mF, is used as the primary and only storage element [39]. The emulation setup is the same as in Fig. 13(b), but now with

another software application running on the STM32WB55 MCU.

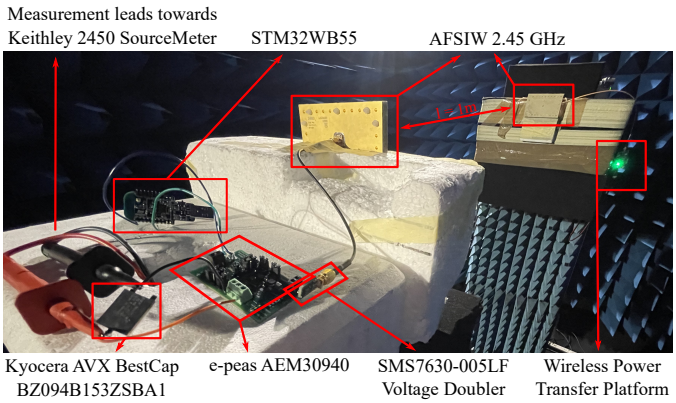

Fig. 19. Measurement setup in the anechoic chamber, for the temperature-monitor application based on RF EH.

To emulate this application correctly, the received RF power at the input of the rectifier was measured with an FSV40 Rohde & Schwarz spectrum analyzer. In this measurement setup, a received power level of -7.4 dBm was obtained.

2) MPP configuration: Based on the simulated I-V curve of the rectifier, the MPP can be configured for this application. For the AEM30940 PMU, this can be set to a V_{oc} ratio of 50%, 65% or 80% [38]. In Fig. 20, the simulated I-V and P-V curves for an input power level of -7.4 dBm is shown, with its corresponding MPPs and the V_{oc} ratios of 50%, 65% or 80%. Based on this curve, the MPP of the rectifier amounts to 45.81%, which is closest to a V_{oc} ratios of 50%.

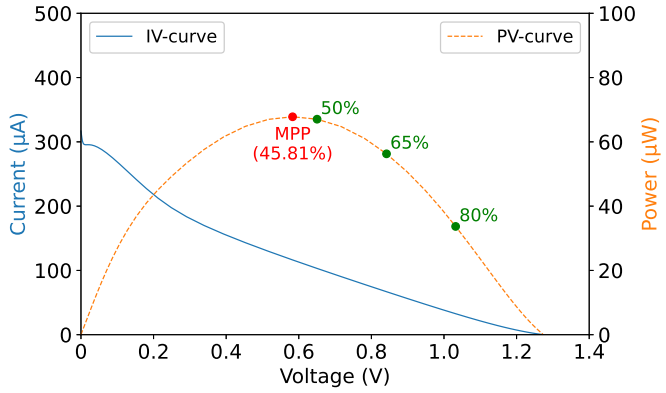

Fig. 20. Simulated I-V and P-V curve of the rectenna for an input power level of -7.4 dBm, annotated with its corresponding MPPs.

3) Optimal Configuration: As in the first example, the optimal configuration was reached with the help of the emulation platform. A maximum packet update rate was obtained with an output voltage of 1.8 V, V_{ovdis} = 2.20 V and V_{chrdy} = 2.32 V. The AEM30940 PMU is now configured as close as possible to this configuration through extra resistors [38]. Again, due to the use of E12 resistor and the tolerances on them, the measured threshold voltages deviate a bit from the ideal configuration: V_{ovdis} = 3.205 V and V_{chrdy} = 3.325 V, which can be noticed in the measured voltage across the supercapacitor in Fig. 21(a). The emulation platform is updated with these new threshold voltages to show the accuracy of the proposed emulation platform again. In addition, in Fig. 21(b), the measured output current by the emulation platform is shown for this optimal configuration.

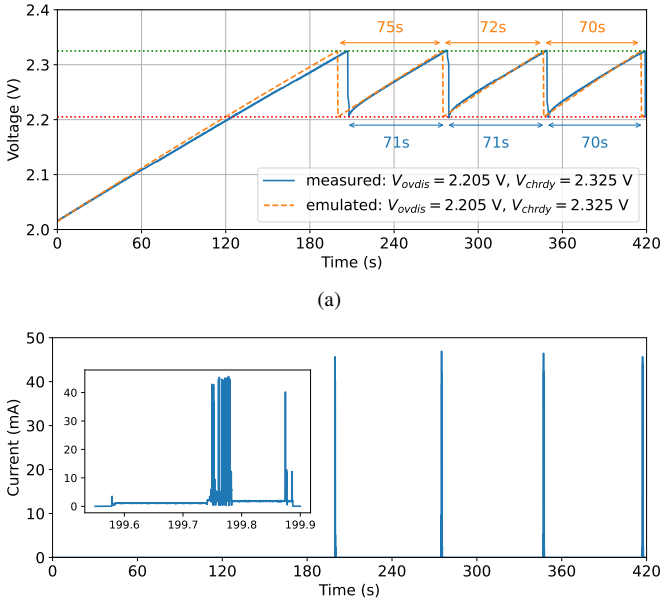

Fig. 21. Optimal configuration: (a) Emulated and measured voltage across the supercapacitor, as a function of time, (b) measured output current by the emulation platform, as a function of time, demonstrating high degree of accuracy in current measurement.

VII. Conclusion

This research demonstrates that the proposed emulation platform effectively replicates the behavior of realistic EH systems, providing a reliable and efficient tool for the development and optimization of EH-powered IoT devices. The results validate its ability to accelerate the design cycle by enabling rapid evaluation of different hardware and software configurations under various energy availability scenarios. Additionally, the platform's accuracy in modeling supercapacitor behavior, including leakage and diffusion currents, ensures precise energy management assessments.

An accurate and realistic digital twin model of each part of a typical EH system is integrated in the emulation platform. These include emulation models for various energy harvesters, a complete and realistic model of the power management system, and a novel and advanced supercapacitor model integrating leakage and diffusion current characteristics. The modular design of the emulator allows for easy extension to other energy sources, such as thermoelectric generators or piezoelectric harvesters, by implementing additional digital-twin models or importing their I-V curves. In addition, a novel add-on hardware shield is developed, providing a programmable and stable output voltage, and containing a very accurate current measuring circuit to support accurate emulation of the complete EH system.

The successful application of the platform in both ambient light and RF energy harvesting scenarios highlights its versatility and practical relevance. By reducing the need for costly and time-consuming hardware iterations, this approach significantly lowers the barriers to EH adoption, particularly for small-scale enterprises. Moving forward, this work establishes a foundation for further advancements in EH system design, contributing to the broader goal of making energy harvesting a viable and widely adopted alternative to traditional battery-powered solutions.

ACKNOWLEDGEMENT

Part of this research was funded by the Flemish FWO SBO S001521N IoBaLeT (Sustainable Internet of Battery-Less Things).

REFERENCES

[1] "Energy Harvesting System Market Analysis - 2030 — Growth Statistics," Allied Market Research, 09 2021. [Online]. Available: https://www.alliedmarketresearch.com/energy-harvesting-system-market-A13686

[2] "Internet of Things Market Size — IoT Industry Forecast - 2030," Allied Market Research, 02 2022. [Online]. Available: https://www.alliedmarketresearch.com/internet-of-things-IoT-market

[3] D. Van Leemput, A. Sabovic, K. Hammoud, J. Famaey, S. Pollin, and E. De Poorter, "Energy Harvesting for Wireless IoT Use Cases: A Generic Feasibility Model and Tradeoff Study," *IEEE Internet of Things Journal*, vol. 10, no. 17, pp. 15 025–15 043, 2023. [Online]. Available: https://ieeexplore.ieee.org/document/10089846

[4] P. De Mil, B. Jooris, L. Tytgat, R. Catteeuw, I. Moerman, P. Demeester, and A. Kamerman, "Design and implementation of a generic energy-harvesting framework applied to the evaluation of a large-scale electronic shelf-labeling wireless sensor network," *Eurasip Journal on Wireless Communications and Networking*, vol. 2010, 2010.

[5] S. Bobovych, N. Banerjee, R. Robucci, J. P. Parkerson, J. Schmandt, and C. Patel, "SunaPlayer: High-accuracy emulation of solar cells," *IPSN 2015 - Proceedings of the 14th International Symposium on Information Processing in Sensor Networks (Part of CPS Week)*, pp. 59–70, 2015.

[6] H. Zhang, M. Salajegheh, K. Fu, and J. Sorber, "Ekho: Bridging the gap between simulation and reality in tiny energy-harvesting sensors," *Proceedings of the 4th Workshop on Power-Aware Computing and Systems, HotPower'11*, 2011.

[7] J. Hester, T. Scott, and J. Sorber, "Demo abstract: Ekho: Realistic and repeatable experimentation for tiny energy-harvesting sensors," *SenSys 2014 - Proceedings of the 12th ACM Conference on Embedded Networked Sensor Systems*, pp. 330–331, 2014.

[8] J. Hester, L. Sitanayah, T. Scott, and J. Sorber, "Realistic and repeatable emulation of energy harvesting environments," *ACM Transactions on Sensor Networks*, vol. 13, no. 2, 2017.

[9] R. P. D. A. Filho, O. A. De Lima, and C. G. Furtado, "An FPGA-based evaluation platform for energy harvesting embedded systems," *Proceedings - 32nd Symposium on Integrated Circuits and Systems Design, SBCCI 2019*, 2019.

[10] K. Geissdoerfer, M. Chwalisz, and M. Zimmerling, "Shepherd: A portable testbed for the batteryless IoT," *SenSys 2019 - Proceedings of the 17th Conference on Embedded Networked Sensor Systems*, pp. 83–95, 2019.

[11] J. De Winkel, T. Hoefnagel, B. Blokland, and P. Pawełczak, "DIPS: Debug Intermittently-Powered Systems Like Any Embedded System," *SenSys 2022 - Proceedings of the 20th ACM Conference on Embedded Networked Sensor Systems*, pp. 222–235, 2022.

[12] F. Mühlbacher, M. Schuß, H. Brunner, and C. Boano, *Demo: A Flexible Extension Board for IoT Devices to Enable their Batteryless Operation*. United States: Association of Computing Machinery, Dec. 2024, 21st International Conference on Embedded Wireless Systems and Networks, EWSN 2024, EWSN'24 ; Conference date: 10-12-2024 Through 13-12-2024. [Online]. Available: https://ewsn24.tii.ae/

[13] L. Smith, T. Ibn-Mohammed, S. L. Koh, and I. M. Reaney, "Life cycle assessment and environmental profile evaluations of high volumetric efficiency capacitors," *Applied Energy*, vol. 220, pp. 496–513, 06 2018.

[14] L. Smith, T. Ibn-Mohammed, D. Astudillo, S. Brown, I. Reaney, and S. Koh, "The role of cycle life on the environmental impact of li6.4la3zr1.4ta0.6o12 based solid state batteries," *Advanced Sustainable Systems*, 11 2020.

[15] T. Ibn-Mohammed, S. Koh, I. Reaney, A. Acquaye, G. Schileo, K. Mustapha, and R. Greenough, "Perovskite solar cells: An integrated hybrid lifecycle assessment and review in comparison with other photovoltaic technologies," *Renewable and Sustainable Energy Reviews*, vol. 80, pp. 1321–1344, 12 2017.

[16] "Solarcell remote™ w/usb-c charging cable — samsung us," Samsung Electronics America. [Online]. Available: https://www.samsung.com/us/televisions-home-theater/television-home-theater-accessories/televisions/solarcell-remote-vg-tm2180es-za/

[17] W. Mrozik, M. Ali Rajaeifar, O. Heidrich, and P. Christensen, "Environmental impacts, pollution sources and pathways of spent lithium-ion batteries," *Energy & Environmental Science*, vol. 14, 10 2021. [Online]. Available: https://pubs.rsc.org/en/content/articlehtml/2021/ee/d1ee00691f

[18] J. K. Øygard, A. Måge, E. Gjengedal, and T. Svane, "Effect of an uncontrolled fire and the subsequent fire fight on the chemical composition of landfill leachate," *Waste Management*, vol. 25, pp. 712–718, 01 2005.

[19] "A strategy for achieving aluminium's full potential for circular economy by 2030." [Online]. Available: https://european-aluminium.eu/wp-content/uploads/2022/08/european-aluminium-circular-aluminium-action-plan.pdf

[20] F. K. Shaikh and S. Zeadally, "Energy harvesting in wireless sensor networks: A comprehensive review," *Renewable and Sustainable Energy Reviews*, vol. 55, pp. 1041–1054, 03 2016.

[21] P. De Mil, B. Jooris, L. Tytgat, R. Catteeuw, I. Moerman, P. Demeester, and A. Kamerman, "Design and implementation of a generic energy-harvesting framework applied to the evaluation of a large-scale electronic shelf-labeling wireless sensor network," *EURASIP Journal on Wireless Communications and Networking*, vol. 2010, 07 2010.

[22] Q. Wen, X. He, Z. Lu, R. Streiter, and T. Otto, "A comprehensive review of miniatured wind energy harvesters," *Nano Materials Science*, 05 2021.

[23] C. Jones and C. Hansen, "Single diode parameter extraction from in-field photovoltaic i-v curves on a single board computer," 06 2019.

[24] "AEM10941, Highly Efficient, Regulated Dual-Output, Ambient Energy Manager for Up To 7-cell Solar Panels with Optional Primary Battery." [Online]. Available: https://e-peas.com/wp-content/uploads/datasheets/ds-aem10941_qfn28-v2-1.pdf

[25] L. Helseth, "Modelling supercapacitors using a dynamic equivalent circuit with a distribution of relaxation times," *Journal of Energy Storage*, vol. 25, p. 100912, 10 2019.

[26] O. Tremblay and L.-A. Dessaint, "Experimental validation of a battery dynamic model for ev applications," *World Electric Vehicle Journal*, vol. 3, no. 2, pp. 289–298, 2009.

[27] "Indoor solar cell TDK BCS4430B6." [Online]. Available: https://product.tdk.com/system/files/dam/doc/product/solar-cell/catalog/film-solarcell_bcs_en.pdf

[28] "313070004 — Seeed Studio 0.5W Kit solar panel — RS," benl.rs-online.com. [Online]. Available: https://benl.rs-online.com/web/p/solar-panels/1793740

[29] "AVX 50 mF 5.5V AVX BZ015A503ZSB." [Online]. Available: https://www.mouser.be/datasheet/2/40/AVX_BestCap-3182019.pdf

[30] "Pulse Sensor." [Online]. Available: https://pulsesensor.com/

[31] "STM32WBx5." [Online]. Available: https://www.st.com/en/microcontrollers-microprocessors/stm32wbx5.html

[32] N. De Raeve, A. Shahid, M. De Schepper, E. De Poorter, I. Moerman, J. Verhaevert, P. Van Torre, and H. Rogier, "Bluetooth-Low-Energy-Based Fall Detection and Warning System for Elderly People in Nursing Homes," *Journal of Sensors*, vol. 2022, no. Ml, 2022.

[33] "Power Profiler Kit II." [Online]. Available: https://www.nordicsemi.com/Products/Development-hardware/Power-Profiler-Kit-2

[34] "2450 Source Measure Unit (SMU) Instrument Datasheet." [Online]. Available: https://www.tek.com/en/datasheet/smu-2400-graphical-sourcemeter/model-2450-touchscreen-source-measure-unit-smu-instrument

[35] J. Sennesael, J. Jocqué, T. Debuysscher, S. Lemey, J. Verhaevert, P. V. Torre, D. Schreurs, and H. Rogier, "Modular platform for efficient wireless power transfer to low-power devices," in *2024 4th URSI Atlantic Radio Science Meeting (AT-RASC)*, 2024, pp. 1–4.

[36] Q. Van Den Brande, S. Lemey, J. Vanfleteren, and H. Rogier, "Highly Efficient Impulse-Radio Ultra-Wideband Cavity-Backed Slot Antenna in Stacked Air-Filled Substrate Integrated Waveguide Technology," *IEEE Transactions on Antennas and Propagation*, vol. 66, no. 5, pp. 2199–2209, 2018.

[37] J. Jocqué, J. Sennesael, J. Verhaevert, P. Van Torre, D. Schreurs, and H. Rogier, "Rectifier optimization for low-power rf energy harvesting tags," in *2024 IEEE International Symposium on Antennas and Propagation and INC/USNC-URSI Radio Science Meeting (AP-S/INC-USNC-URSI)*, 2024, pp. 17–18.

[38] "AEM3040, Highly Efficient, Regulated Dual-Output, Ambient Energy Manager for AC or DC Sources with Optional Primary Battery." [Online]. Available: https://e-peas.com/wp-content/uploads/datasheets/ds-aem30940_qfn28-v1-6.pdf

[39] "AVX 15 mF 4.5V AVX BZ094B153ZSBA1." [Online]. Available: https://www.mouser.be/datasheet/2/40/AVX_BestCap-3182019.pdf